ACS Catalysis

pubs.acs.org/acscatalysis

Research Article

Resolving Activation Entropy of CO Oxidation under the Solid−Gas and Solid−Liquid Conditions from Machine Learning Simulation

Ling-Heng Luo, Si-Da Huang, Cheng Shang,* and Zhi-Pan Liu*

Cite This: *ACS Catal.* 2022, 12, 6265−6275

Read Online

ACCESS | Metrics & More | Article Recommendations | Supporting Information

ABSTRACT: The free-energy barrier and its temperature dependence and the activation entropy of chemical reactions are key quantities to reaction kinetics but are very challenging to predict accurately, particularly for reactions in complex environments. Herein, by combining global neural network potential with umbrella sampling molecular dynamics (MD), we are able to resolve the activation entropy of CO oxidation on Pt(111), a prototype heterogeneous catalytic reaction, with two different mechanisms (CO reacting with the adsorbed atomic O, CO + O, and with the adsorbed OH, CO + OH) in the absence and presence of an aqueous solution. We show that (i) CO + OH reaction is always kinetically more preferable than CO + O reaction despite that the presence of an aqueous solution increases significantly the barrier of CO + OH reaction, and (ii) the activation entropy, although with the absolute value being below 35 J·mol^{-1}·K^{-1}, equivalent to 0.1 eV at 300 K, contributes differently to the free-energy barrier depending on the reaction conditions: it is negative under the solid−gas conditions but turns out to be positive under the solid−liquid conditions. The configuration entropy dominates the activation entropy, to which the classic harmonic approximation to account for the vibrational entropy is a poor approximation. Our results are of significance for understanding and predicting the free-energy barrier of catalytic recombination reactions in general.

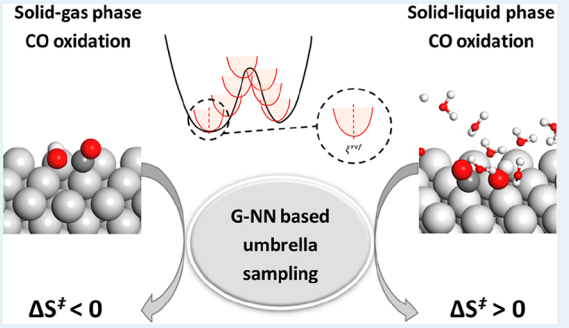

KEYWORDS: *machine learning, free-energy calculation, activation entropy, CO oxidation, solid−liquid interface, neural network potential, electrocatalysis*

1. INTRODUCTION

CO oxidation on Pt is a model heterogeneous catalytic reaction extensively studied in the past decades.[1] The reaction is not only of great importance under the solid−gas conditions, for example, used in automobile exhaust treatment,[2−6] but also commonly encountered under the solid−liquid conditions, for example, for electrocatalysis on Pt electrodes.[7,8] Despite tremendous efforts made in understanding the catalytic reaction, many challenges remain to be solved, particularly on enhancing the room-temperature activity and on reducing the CO poisoning under the solid−liquid reaction conditions. It is the purpose of this work to understand this fundamentally important reaction under different catalytic conditions, that is, with and without an aqueous solution, by using the latest-developed machine-learning potential-based atomic simulation.

Taking the reaction on single-crystal Pt(111) as an example where surface science experimental data are most available, we summarize key findings on this reaction below. The reaction has complex kinetics behaviors with multiple temperature regimes of CO_2 production, categorized as the low-temperature reaction (~220 K) and the high-temperature reaction (~340 K). The low-temperature reaction occurs exclusively at O island peripheries, and a trace of H_2O can significantly promote the reaction.[9,10] The fitted reaction barrier by near-edge X-ray absorption fine structure spectroscopy (NEAXFS) experiments is as low as 0.31 eV with a substantially low pre-exponential factor of 10^2 s^{-1},[11] while it is 0.53 eV with a 10^6 s^{-1} pre-exponential factor by *in situ* high-resolution X-ray photoelectron spectroscopy.[12] At high temperatures, the reaction is reasonably attributed to CO reacting with the isolated O atom. The activation barrier reported, however, is highly scattered, varying from a low value of 0.39−0.51 eV measured by variable-temperature scanning tunneling microscopy,[13] NEAXFS,[11] and molecular beam (MB)[14,15] experiments to a high value of 0.74−1.05 eV from temperature-programmed desorption[16] and MB[15] experiments. Accordingly, the pre-exponential factor is also in a wide range from 10^4 to 10^8 s^{-1} (suggesting a negative activation entropy).[11,13−15]

To understand the experimental findings, the reaction has also been extensively studied in theory. Some studies focused on the CO adsorption puzzles where CO is observed dominantly at the

Received: March 31, 2022
Revised: April 28, 2022

https://doi.org/10.1021/acscatal.2c01561
ACS Catal. 2022, 12, 6265−6275

top sites in experiments but tends to favor the high coordination sites [face-centered cubic (fcc) hollow sites] using density functional theory (DFT) calculations. For example, CO adsorption at the fcc hollow site is ∼0.17 eV more stable than that at the top site (0.11 ML) with the DFT Perdew−Burke−Ernzerhof (PBE) functional.[17]

The others aimed to resolve the reaction mechanism and kinetics, which showed that the calculated reaction barrier for CO reacting with atomic O is high, that is, 0.74−1.06 eV (depending on DFT functionals), in a $p(2 \times 2)$ supercell (0.25 ML) where CO is initially at the top site and O is at the fcc hollow site.[18−21] Apparently, the high barrier of CO + O cannot explain the low temperature activity. Instead, the CO + OH mechanism is proposed to be responsible at low temperatures, where the reaction barrier is calculated to be ∼0.4 and 0.60 eV without and with H_2O molecules near OH,[20,22] respectively.

The major inconsistency in the field is on the pre-exponential factor of CO oxidation, leading to the large uncertainties on the activation entropy. Based on transition state (TS) theory, the pre-exponential factor of CO + O and CO + OH reaction was calculated to be $1.5-11.2 \times 10^{12}$ s^{-1} (0.25 ML) and 9.89×10^{12} s^{-1}, respectively, from DFT with the harmonic approximation to obtain the vibrational frequency for both the initial state (IS) and TS.[19,20] Recently, the complete potential energy sampling method[23] was further utilized to refine the translation entropy of adsorbed CO, and a pre-exponential factor of 3.3×10^{10} (interpolated to zero coverage) s^{-1} was obtained. These theoretical values are generally larger than the data fitted from experiments, for example, 10^9 s^{-1} for high-temperature CO oxidation by Nakai et al.[11]

On the other hand, at the solid−liquid (Pt−H_2O) interface, CO oxidation on a Pt electrode cannot occur readily under the ambient conditions, commonly known as the CO poisoning phenomenon. In practice, the elevation of electrochemical potential is essential to promote the reaction: on Pt(111), the CO oxidation starts at 0.7 V *versus* RHE (the same reference hereafter) and exhibits a narrow main peak at 0.75−0.8 V in 0.1 M H_2SO_4/$HClO_4$ and ∼0.8 V in 0.1 M NaOH.[24,25] When the temperature increases to 328 K, the starting potential for CO electro-oxidation reduces slightly to 0.68 V.[26] The electro-oxidation of CO on the Pt electrode was suggested to be mediated by the carboxyl (COOH) intermediate according to shell-isolated nanoparticle-enhanced Raman spectroscopy (SHINERS).[25] Since the carboxyl intermediate should come from the recombination of CO with OH, it is intriguing why the CO + OH reaction turns out to be difficult at the solid−liquid interface compared to the solid−gas conditions occurring at low temperatures. In addition, DFT calculations with modified Poison−Boltzmann electrostatics for treating the solvation and surface charging showed that the barriers of surface recombination reactions are insensitive to the electrochemical potential[27] but can be influenced strongly by the local coverage of adsorbates. It thus suggests that CO + OH reaction in solution is likely to have a much higher barrier than under the solid−gas conditions.

To settle the long-standing puzzles on CO oxidation under different reaction conditions, herein, we systematically investigate CO oxidation in the absence and presence of an aqueous solution *via* machine-learning-based atomic simulation. A Pt−C−H−O quaternary global neural network (G-NN) potential[28,29] is developed to allow for long-time enhanced molecular dynamics (MD) simulations, namely, umbrella sampling (US),[30] in computing the free-energy profiles for CO reacting with atomic O and with OH in both solid−gas and solid−liquid environments, that is, CO + O(g), CO + OH(g), CO + O(aq), and CO + OH(aq) (g and aq stand for gas and aqueous solution, respectively). Based on the free-energy profiles at different temperatures, we provide new physical insights into CO oxidation under different reaction conditions. The activation entropies of CO oxidation are obtained and discussed in the context of previous findings.

2. METHODS

2.1. G-NN Potential Generated from the SSW-NN Method. To perform the long-time atomic simulation for CO oxidation under different reaction conditions, we utilized the latest machine learning techniques to generate a Pt−C−H−O quaternary G-NN potential as implemented in the Large-scale Atomic Simulation with neural network Potential (LASP, www.lasphub.com) program developed by our group. The G-NN potential follows the atom-centered high-dimensional NN architecture[28,31] and utilizes the power-type structure descriptor (PTSD)[29] as the input layer for NN, which consists of 170 two-body, 200 three-body, and 40 four-body PTSDs for each element. The G-NN potential is generated by self-learning the global potential energy surface (PES) data set screened from G-NN-based stochastic surface walking (SSW)[32,33] global optimization, namely, the SSW-NN method. The final data set contains 79,724 structures that are computed by DFT, including bulks, layers, clusters, and surfaces, and the final accuracy for the G-NN potential is 3.229 meV/atom for the root-mean-square (RMS) error in energy and 0.111 eV/Å for the force. The Pt−C−H−O G-NN potential is openly available on the LASP website (*via* the link[34]). More details of the G-NN potential architecture and SSW-NN method can be found from Table S1 in the Supporting Information. The typical accuracy of G-NN potential is illustrated in Figure 1a, where the benchmark with DFT results is shown for 18 structures randomly selected from the umbrellas sampling the MD trajectory of the CO + OH(aq) reaction pathway (the RMS error in energy is 0.068 eV per slab of 188 atoms). More benchmarks are detailed in Table S3.

2.2. Free-Energy Calculation and the Derivation of Reaction Entropy Contribution. The free-energy profiles for CO oxidations under different reaction conditions were obtained by performing enhanced MD simulations based on G-NN potential using the LASP program. All MD simulations were carried out in the canonical ensemble with a Nose−Hoover thermostat under 300−500 K for the solid−gas reactions and 300−380 K for solid−liquid reactions, both with a small time step of 0.1 fs interval. The free-energy profile was calculated using a US method, a bias MD method to obtain the mean force along the reaction coordinate. The reaction coordinate is divided into 60−80 windows distributed evenly along the reaction pathway from IS to FS. This is achieved by imposing the harmonic bias potential $\omega_i = \frac{K}{2}(\xi - \xi_i^{\mathrm{ref}})^2$ to constrain a designated reaction coordinate ξ_i^{ref} for each window i. As shown in eq 1, the resulting biased probability at each window $P_i^{\mathrm{b}}(\xi)$ can be collected from MD simulation

$$P_i^{\mathrm{b}}(\xi) = \frac{\int \exp\{-\beta[E(r) + \omega_i(\xi'(r))]\}\delta[\xi'(r) - \xi]\mathrm{d}^N r}{\int \exp\{-\beta[E(r) + \omega_i(\xi'(r))]\}\mathrm{d}^N r} \quad (1)$$

The derivative of free energy to the reaction coordinate ξ, $\partial G_i/\partial\xi$, can be derived as shown in eq 2.[35] The umbrella

https://doi.org/10.1021/acscatal.2c01561
ACS Catal. 2022, 12, 6265−6275

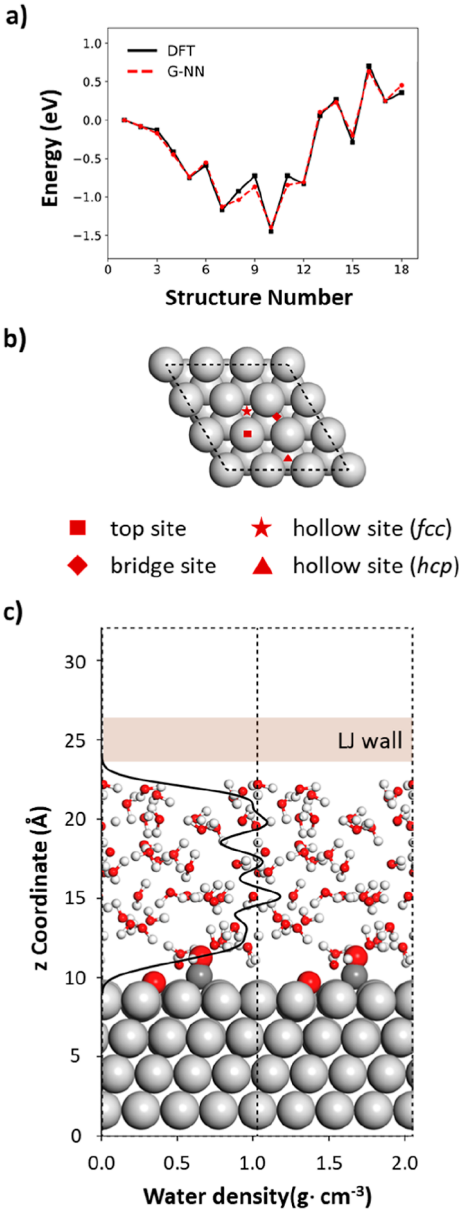

Figure 1. (a) Benchmark of G-NN potential and DFT energetics for 18 structures randomly selected from the US MD trajectory of the CO + OH(aq) reaction pathway. The energy is relative to the initial structure. (b) Top view of a $p(3 \times 3)$ supercell of the Pt(111) surface. (c) The side view for the Pt(111)/H_2O interface for modeling CO + O(aq) reaction. The density profile of water layers (4 layers) at equilibrium is also shown in the black curve. The average density of ∼1.0 g·cm^{-3} of water is achieved *via* a soft confinement potential (LJ repulsive potential).

integration method was utilized to approximate the $\partial G_i/\partial\xi$ and integrate the potential of mean force to finally export the free-energy ΔG profile

$$\frac{\partial G_i}{\partial \xi} = \frac{1}{\beta}\frac{\xi - \overline{\xi_i^{\mathrm{b}}}}{(\sigma_i^{\mathrm{b}})^2} - K(\xi - \xi_i^{\mathrm{ref}}) \tag{2}$$

where $\overline{\xi_i^{\mathrm{b}}}$ represents the mean value of ξ and σ_i^{b} represents the variance. In this work, the reaction coordinate ξ is defined as the distance between the C and the reacting O(H), and it is rescaled into the range of 0−1, with IS and FS corresponding to 0 and 1, respectively.

In the constant temperature MD simulation, the Nose−Hoover mass is set in the range of 0.6 to 1 eV·fs^2 for the solid−gas reactions and 400 to 800 eV·fs^2 for the solid−liquid reactions, adjusted at different windows to guarantee the temperature control and energy conservation. The force constant K (eq 2) for the harmonic bias potential is also adjusted from 30 to 50 eV·Å^{-2} for different temperatures in order to keep the appropriate overlap of ξ between windows.

The starting structures in each window of US are generated from the trajectory with the lowest free-energy barrier by pre-running a number of US trajectories. The simulation time for each window is 5 ps for the solid−gas and 10 ps for solid−liquid reactions, with the initial 40% of time for equilibrium and the rest for production. Each free-energy profile is averaged from five times of US simulations to ensure the credibility of the data (see Table S4 for the data).

Once the free-energy barrier of reaction G_a is obtained at a series of temperatures, we can use the rate constant k and temperature to generate the ln $k-T$ Arrhenius plot, and thus, the activation energy E_a, the pre-exponential factor A, and the activation entropy $\Delta S^{\ddagger}$ can be fitted/derived according to the TS theory as shown in eq 3

$$k = \frac{k_B T}{h} e^{G_a/RT} = \frac{k_B T}{h} e^{\Delta S^{\neq}/R} e^{-E_a/RT} = A\, e^{-E_a/RT} \tag{3}$$

In this work, the pre-exponential factor A and the activation entropy ($\Delta S^{\ddagger}$) derived at 300 K are utilized for comparison between reactions.

2.3. Models for Reactions. *2.3.1. Pt(111).* The Pt(111) surface is modeled by a four-layer slab with the bottom two layers of atoms being fixed at the bulk position. The top view of the surface in a $p(3 \times 3)$ supercell is shown in Figure 1b, with the typical adsorption sites on the (111) surface, including top, bridge, and hollow [fcc and hexagonal close-packed (hcp)] sites, as labeled.

2.3.2. Pt−H_2O Interface. The reactions in the aqueous surroundings are simulated in the $p(4 \times 2\sqrt{3})$ Pt(111) supercell with 40 explicit water molecules on top of the surface (see Figure 1c). The water layers are restricted to the surface by a Lennard-Jones (LJ) wall potential positioned in vacuum to ensure the density of water at ∼1.0 g·cm^{-3}. The O−H bonds in system are restrained to their equilibrium distance (1.0 Å) using a Gaussian bias potential. The constraining of O−H bond distance can facilitate to obtain the averaged free-energy profile of CO + OH reaction in aqueous solution, which, if without the constraint, has a chance to decay to CO + O reaction by losing its H of reacting OH to solution. We have confirmed that the extra constraints do not introduce systematic error to the reaction barrier of CO + OH reaction. To equilibrate the reaction in aqueous solution, we start from the most stable structure from SSW-NN global optimization (see Section 2.4 below) and then perform long-time MD (800 ps) for the reactions at the ISs. The density profile of water layers along the z-axis after equilibrium is also shown in Figure 1c, which agrees well with previous works using *ab initio* MD (AIMD) simulation.[36,37]

2.4. DFT Calculations and Reaction Pathway Search. For the solid−gas reactions, DFT calculations are carried out to compute the reaction profile as implemented in the Vienna ab initio simulation package (VASP).[38−40] The DFT calculation

https://doi.org/10.1021/acscatal.2c01561
ACS Catal. 2022, 12, 6265−6275

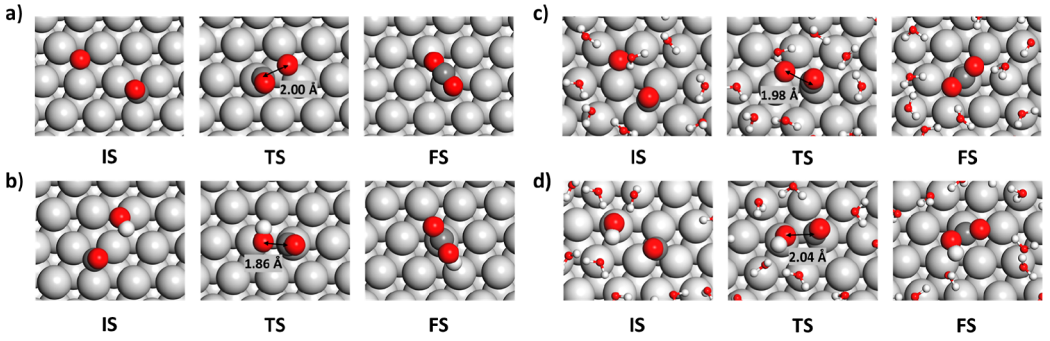

Figure 2. Reaction snapshots, including IS, TS, and FS, from MD simulations: (a) CO + O(g) at 0.11 (1/9) ML CO and 0.11 ML O coverage. (b) CO + OH(g) at 0.11 ML CO and 0.11 O ML coverage. (c) CO + O(aq) at 0.06 (1/16) ML CO and 0.06 ML O coverage. (d) CO + OH(aq) at 0.06 (1/16) ML CO and 0.06 ML OH coverage. In (c,d), only the first layer of water is shown for clarity. Atom representation scheme: big gray ball: Pt; small gray ball: C; red ball: O; white ball: H.

Table 1. Structural Statistics for Four CO Oxidation Reactions from MD Trajectories[a]

	CO site		O/OH site		C−O distance	
reaction	IS	TS	IS	TS	IS	TS
1	b (53%) + h (47%)	t (100%)	h (100%)	b (100%)	4.87	2.00
2	h (66%) + b (34%)	t (100%)	t (90%) + b (10%)	t (100%)	3.54	1.86
3	b (51%) + h (49%)	t (100%)	h (100%)	b (100%)	3.44	1.98
4	h (97%) + b (3%)	t (100%)	t (100%)	t (100%)	3.54	2.04

[a]Listed data include the CO, O, and OH population (%) at different surface sites and the average C−O distance (Å) at the IS and TS at 300 K. Notation b: bridge, h: hollow, and t: top site. Reactions 1−4 refer to CO + O (g), CO + OH (g), CO + O (aq), and CO + OH (aq), respectively.

setup is the same as the data set creation used in G-NN potential generation. Specifically, the projected augmented wave potential is utilized to represent the electron−ion interaction, and the DFT exchange−correlation functional utilized is the PBE functional, widely applied for reactions on metals.[41,42] The van der Waals (vdW) effect is also checked by adding Grimme's D3 vdW correction[43] in MD simulation, which is found to have little effect on the free-energy barrier (<0.03 eV). The kinetic energy cutoff is set as 450 eV. The first Brillouin zone *k*-point sampling utilizes the Monkhorst−Pack scheme with an automated mesh determined by 25 times the reciprocal lattice vectors.

The SSW-NN method is employed to search for the global minimum of IS for all reactions at 0 K (see Table S2). The reaction pathway search is then obtained by using the double-ended surface walking[44] method and refined using constrained Broyden minimization[45] to locate the TS. All minima IS and TS are confirmed by vibrational frequency analysis, that is, no imaginary frequency for IS and one for TS.

3. RESULTS

3.1. Reaction under the Solid−Gas Conditions.

3.1.1. CO + O(g) Reaction. Our investigation starts from CO + O on Pt(111) by using the G-NN potential to explore different possible configurations and perform free-energy calculations. Two different surface coverages are initially considered in SSW-NN simulation to identify the best initial configuration, which shows that in accordance with the literature,[17] CO prefers the fcc hollow sites at the low coverage (0.11 ML CO and 0.11 ML O), as shown in Figure 2a, and shifts to the top site at the relative high coverage (0.25 ML CO and 0.25 ML O). This is due to the well-known deficiency of the DFT PBE functional in predicting CO adsorption sites at low coverages (the energy difference is 0.17 eV between CO at the fcc hollow site and at the top site at the PBE functional using VASP). This should not affect us to compare systematically CO oxidation under different reaction conditions at the same DFT level. As we focus on the catalytic reaction under different conditions, the results at the low coverage limit, 0.11 ML CO and 0.11 ML O (see in Figure 1b), will be presented in detail. We will return to the effect of CO adsorption sites on free energy in the discussion section (Section 4.2).

The lowest reaction pathway at 0 K for CO reacting with O is first searched, and the lowest energy TS has a bent CO−O structure over the fcc hollow site with CO at the atop site and O at the bridge site; the C−O distance is 1.99 Å (*cf.* 2.02−2.07 Å in the literature[19,21]). The calculated reaction barrier is 0.92 eV with respect to CO at the fcc hollow site and reduced to 0.74 eV with respect to CO at the top site. These values are consistent with the data reported previously.[18−21]

Next, the free-energy profiles for the reaction have been calculated using enhanced MD simulation based on the US method. Five different temperatures (from 300 to 500 K) are investigated, and the free-energy barriers are calculated, and the barrier is 0.96 eV at 300 K and increases slightly to 0.99 eV at 500 K. Figure 2a shows the most common snapshots from MD at 300 K, and Table 1 lists the related structural information. We note that under the solid−gas reaction conditions, the FS state CO_2 of CO oxidation is at a linear form (Figure 2a), which is at least 7 Å away from the surface. Figure 3a shows the free-energy profile at 300 K, collected from 60 windows in US.

We found that at the finite temperatures, the reaction pathway is largely like that at 0 K, except that CO can diffuse rapidly on the surface as manifested by the 53% population of bridge site adsorption and 47% of fcc site adsorption (statistics from a long MD of 100 ps simulation at the IS). The TS structure averaged from the highest energy window along the free-energy profile has the geometry very close to that at 0 K, except that CO−O is now over the hcp site with the OC−O distance being 2.00 Å (Figure 2a) (note that at 0 K, the two different TSs, the TS over the fcc and the TS over the hcp site, differ by 0.05 eV).

https://doi.org/10.1021/acscatal.2c01561
ACS Catal. 2022, 12, 6265−6275

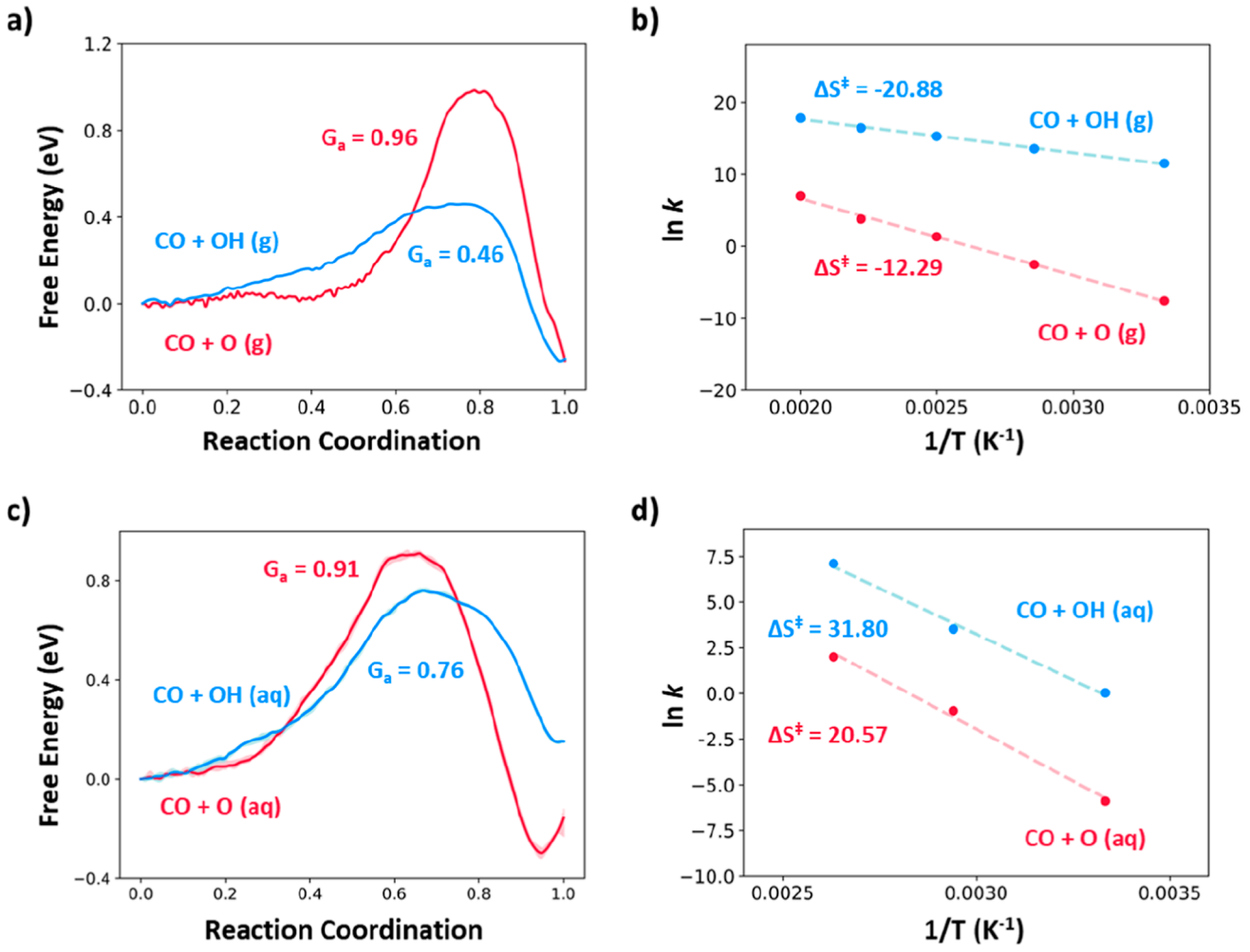

Figure 3. (a) Free-energy profiles for CO + O(g) (red) and CO + OH(g) (blue) reactions on Pt(111) from US MD. (b) Linear fitted Arrhenius plot using the average free-energy barrier at 300−500 K. (c) Free-energy profiles for CO + O(aq) (red) and CO + OH(aq) (blue) reactions on Pt(111) from US MD. (d) Linear fitted Arrhenius plot using the average free-energy barrier at 300−380 K. The unit is eV for the free-energy barrier (G_a) and J·mol^{-1}·K^{-1} for the activation entropy ($\Delta S^{\ddagger}$).

The Arrhenius plot is then obtained as shown in Figure 3b, where the apparent activation barrier and the activation entropy are derived from the linear fit (see eq 3 in Section 2.2). These data are summarized in Table 2, and for comparison, the calculated vibrational entropy at 300 K with the harmonic approximation is also listed.

As shown in Table 2, the fitted activation barrier is 0.92 eV, being 0.05 eV lower than the barrier at 0 K, and the pre-exponential factor is 1.48×10^{12} s^{-1}, which is in the range of the values calculated previously, that is, $1.5-11.2 \times 10^{12}$ s^{-1}.[19,20] Importantly, the activation entropy is negative, −12.29 J·mol^{-1}·K^{-1}, while the vibrational entropy is very small and positive, 0.60 J·mol^{-1}·K^{-1}. The large difference between the activation entropy and the vibrational entropy from the harmonic approximation suggests that the major contribution of activation entropy does not originate from the vibrational degrees of freedom.

Table 2. Key Kinetics Parameters of the Four Reactions[a]

reaction	G_a	E_a, A	$\Delta S^{\ddagger}$	ΔS_{vib}
1	0.96 ± 0.04	0.92, 1.48×10^{12}	−12.29	0.60
2	0.46 ± 0.02	0.40, 5.26×10^{11}	−20.88	−0.84
3	0.91 ± 0.01	0.97, 7.69×10^{13}	20.57	−2.06
4	0.76 ± 0.01	0.86, 2.97×10^{14}	31.80	−0.37

[a]Listed data include the free-energy barrier (eV), the fitted activation barrier (eV), the pre-exponential factor, the activation entropy (J·mol^{-1}·K^{-1}), and the vibrational entropy at 300 K (J·mol^{-1}·K^{-1}). Reactions 1−4 are as the same as Table 1.

3.1.2. CO + OH(g) Reaction. We then move to CO + OH reaction at the solid−gas interface, where the reactant O is replaced with OH. This elementary reaction is of interest by its own, for example, involved in water gas shift reaction to form a carboxyl (COOH) intermediate.[10,46,47] By following the same procedure, we identify the most stable configuration for CO and OH coadsorption, the lowest reaction pathway, and the free-energy profiles. Here, we highlight the major findings by comparing the two reactions with O and OH.

(i) For the IS, being different from O that stays always in the hollow site, OH can diffuse quite freely on the surface from the top site (90% population) to the bridge site (10%). In achieving the TS, the OH is at the top site in the CO + OH reaction (see Figure 2b) for CO + OH TS, which is different from the bridging O at the TS of CO + O reaction. A shorter TS distance of 1.86 Å is found in CO

https://doi.org/10.1021/acscatal.2c01561
ACS Catal. 2022, 12, 6265−6275

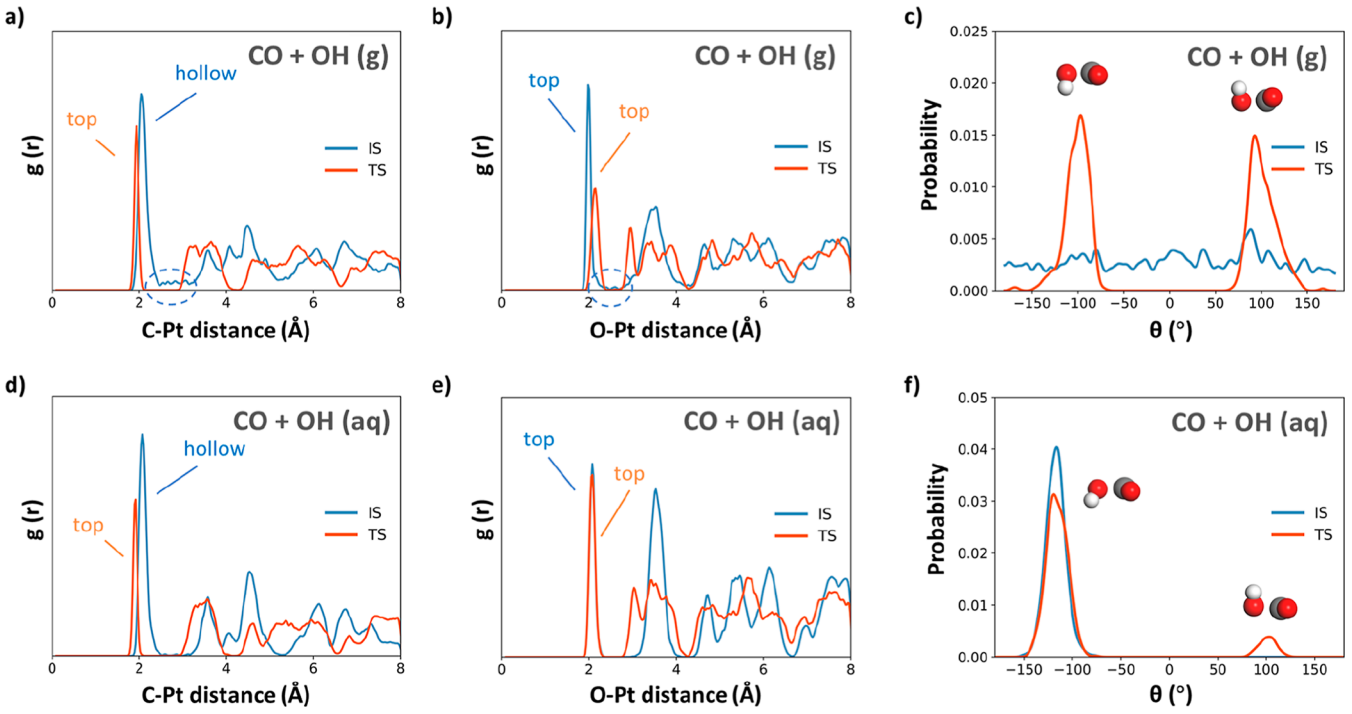

Figure 4. Plots to reflect the structure evolution from IS to TS for CO + OH(g) [the top panel, (a−c)] and CO + OH(aq) [the bottom panel, (d−f)]. (a,d) RDF $g(r)$ for C with its neighboring Pt; (b,e) $g(r)$ for O of OH with its neighboring Pt. (c,f) Rotation angle of OH with respect to the OC−O plane. The dashed circles highlight the tail feature, showing the diffusion of CO/OH.

+ OH reaction, apparently because the top site OH is more inert than the bridging atomic O.

(ii) The reaction energy barrier at 0 K is very low, 0.36 eV, much lower than that of CO + O (0.97 eV). This reflects the fact that the OH activation from IS to TS is much easier compared to the O activation: the atomic O has a corrugated PES with a large energy difference between the fcc hollow site at the IS and the bridge site at the TS.

(iii) The free-energy barrier for CO + OH at 300 K is 0.46 eV, again much lower than that of CO + O. From the Arrhenius plot, we derive the pre-exponential factor to be 5.26×10^{11} s^{-1}, and the activation barrier is 0.40 eV. As a result, an activation entropy of −20.88 $J \cdot mol^{-1} \cdot K^{-1}$ is obtained, which is even more negative than that in CO + O reaction.

To summarize, for the two solid−gas reactions, the entropy at the IS (S_{IS}) is always larger than the entropy at the TS (S_{TS}). As a result, the entropy term of the two solid−gas reactions ($-T\Delta S^{\ddagger}$) contributes positively to the overall free-energy barrier $\Delta G^{\ddagger}$ with a magnitude of up to +0.05 eV at 300 K. In particular, the entropy term in CO + OH reaction is almost double of that in CO + O reaction. Since the vibrational entropy computed using harmonic approximation cannot account for, even qualitatively, the activation entropy, the other entropy terms, the configurational, translational, and rotational entropies, are thus more important for consideration. We further note that for the CO + O and CO + OH reactions, there are in fact no very low vibrational frequencies (*i.e.*, below 50 cm^{-1}) at both the IS and TS (see Supporting Information Table S5) from harmonic vibrational analysis, which suggests that the hindered translation and rotation often discussed in the literature, particularly important for organic molecules (*e.g.*, methanol),[48] should not be the major contributors to the activation entropy in CO oxidation, although they have been taken into account naturally in our MD sampling. Therefore, we conclude that the configurational entropy should be the main source for the activation entropy.

It is of interest to compare the pre-exponential factor from our work with the calculated values in the literature. The activation entropy for CO oxidation on Pt(111) under the solid−gas conditions has been calculated previously by many groups with harmonic approximation,[19,20,23] and the theoretical results generally predict the reaction pre-exponential factor of around 10^{12} s^{-1} ($1.5-11.2 \times 10^{12}$ s^{-1}, close to $k_B T/h = 6.25 \times 10^{12}$ s^{-1} at 300 K), which is in the same order of magnitude as the value from this work (1.48×10^{12} s^{-1}). Jørgensen and Grönbeck[23] have estimated the entropy for CO oxidation reaction using the hindered translator model, which yields a pre-exponential factor of 6.3×10^{10} s^{-1}, in the same order of magnitude as that using a complete potential energy sampling method (3.3×10^{10} s^{-1}). Their calculations consider only the CO diffusion at the IS but neglects the entropy contribution at the TS. These values are smaller than the value (1.48×10^{12} s^{-1}) from our MD results.

3.1.3. MD Trajectory Analysis. To better understand the negative activation entropy, here, we utilize the CO + OH reaction as the example to analyze how the structure configuration evolves from IS to TS. To this end, the long-time (100 ps) MD trajectories at the IS and the TS windows are collected and their geometries are analyzed statistically. The radial distribution function (RDF), $g(r)$, is calculated for the reacting C in CO, $g_{C-Pt}(r)$, and the adsorbed O in OH (O_a), $g_{O-Pt}(r)$, by using eq 4

$$g_{A-B}(r) = \frac{V}{N_B} \frac{\frac{1}{N_A}\sum_{i=1}^{N_A} n_{B_i}}{4\pi r^2 \Delta r} \quad (4)$$

where A represents the centering atom and B is the neighboring atom of A, and n_{B_i} is the number of B within r to $r + \Delta r$ to A.

https://doi.org/10.1021/acscatal.2c01561
ACS Catal. 2022, 12, 6265−6275

Here, $g(r)$ was normalized by dividing the total number of B atoms and the volume of the slab (V).

The $g_{C-Pt}(r)$ is shown in Figure 4a, which can reflect the interaction of C with the Pt(111) surface at the IS (the blue line) and the TS (the orange line). It shows that there is a long tail (the dotted circle in Figure 3a) for the first large peak at 2.1 Å (corresponding to the hollow site adsorbed CO) at the IS, which is caused by the rapid swap between the hollow and neighboring bridge sites (from the hollow site to the bridge site, one C−Pt bond is broken with the distance lengthened from 2.1 to 2.5 Å). This phenomenon is consistent with the population statistics in Table 1. In contrast, the $g_{C-Pt}(r)$ at the TS has a sharp first peak at 1.9 Å with a much lower intensity, which corresponds to the CO exclusively at the top site in reacting with OH. Similarly, we found that in the $g_{O-Pt}(r)$ plot, the first peak also has a small tail, as indicated by the dotted circle in Figure 4b, where the leading peak comes from the top site adsorbed OH (90% population) and the tail caused by the OH diffusion to the bridge site (10% population). At the TS, the O_a is largely fixed at the top site with only a single peak at 2.1 Å. Since both C and O_a are much less mobile at the TS than at the IS, the translational configuration entropy at the TS should be much reduced compared to the IS.

Furthermore, we found that the rotational entropy due to the rotation of the OH bond also contributes to the negative activation entropy. Figure 4c counts the probability of the adsorbed OH at different rotation angles from −180 to 180° with respect to the OC−O plane as a mirror (outward or inward of the plane). We found that the OH can rotate quite freely at the IS with a broad distribution of rotation angles, but at the TS, the angles are limited to two peaks, ∼−100 or ∼100°. Obviously, the OH at the TS has to free an sp^3-hybridized orbital of O_a for reacting with the coming 5σ orbital of the CO molecule.[49,50]

The above analysis from MD trajectories confirms that the TS of the catalytic reaction can only be achieved at a right geometry and thus loses degrees of freedom in translation and rotation. For the CO + OH reaction, not only the adsorption sites for reactants are fixed (*e.g.*, CO and OH at the top site) but also the OH bond is only allowed to point to two specific directions. The reductions of both translational and rotational configuration entropies contribute to the negative activation entropy. With this knowledge, it becomes straightforward to understand why the activation entropy for CO + O reaction is only about half of that for CO + OH reaction: in the CO + O reaction, only one reactant, CO, is mobile at the IS (the O is always at the hollow site), but in the CO + OH reaction, both CO and OH are mobile.

3.2. Reaction in Aqueous Solution. CO oxidation can also occur on Pt electrodes in aqueous solution, where the surrounding H_2O is not merely the solution but also acts as the reactant to provide OH or O at elevated electrochemical potentials.[22] The previous calculations[51] have shown that both OH and O species are available at elevated potentials from thermodynamics following the sequential reaction $H_2O \rightarrow OH + H^+ + e$ and $OH \rightarrow O + H^+ + e$. The former reaction starts ∼0.4 V *versus* RHE, and the latter occurs above ∼0.6 V on Pt(111). It remains elusive on which reaction CO + O(aq) and CO + OH(aq) dominate the electrochemical CO oxidation.

To provide a quantitative answer, we carried out US MD simulation to compute the free-energy profiles for CO reaction with O and OH on Pt(111) in aqueous solution. Three different temperatures (300, 340, and 380 K) have been considered to establish the Arrhenius plot. The reaction snapshots are shown in Figure 2c,d. It is interesting to note that the FS structure for CO + O reaction in aqueous solution has a bent O−C−O structure well adsorbed on the surface, suggesting that FS is more like an adsorbed COO^- stabilized by solution. This is in contrast with the linear form of CO_2, as found in the CO + O(g) reaction in Figure 2a. Figure 3c shows the free-energy profile *versus* the reaction coordinate for CO + O(aq) (red curve) and CO + OH(aq) (blue curve) reaction at 300 K from 80 windows of MD simulation. The statistics on the adsorption site of reactants and the key distances at the ISs and the TSs are also listed in Table 1.

For the IS of CO + O reaction in aqueous solution, we found that similar to it under the solid−gas conditions, CO also has two possible adsorption sites, the hollow site and the bridge site, and the relative population is also close. Again, the adsorbed O stays exclusively at the hollow site (see Table 1). These suggest that the water surroundings do not affect much the adsorption of CO and O in the CO + O reaction.

On the other hand, for the CO + OH reaction, the adsorbed OH always stays at the top site in the aqueous solution, while it swaps between two possible sites (top and bridge) under the solid−gas conditions. From the IS snapshots, the water solution is found to stabilize the top OH (see Figure 5a) *via* H-bondings,

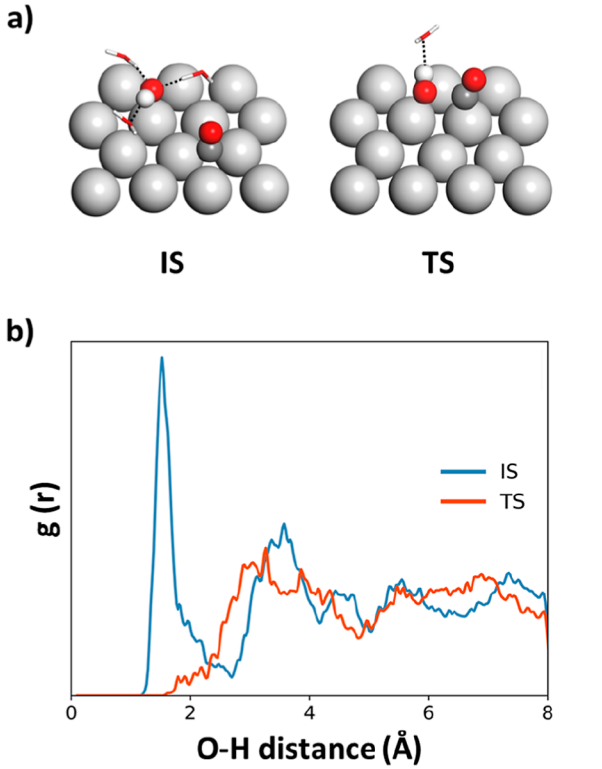

Figure 5. (a) Local H-bonding network at IS and TS in CO + OH(aq) reaction. (b) RDF $g(r)$ for the O of OH with the neighboring H atoms of H_2O.

where the OH acts as both the acceptor and donor of H-bonding. Interestingly, CO now mainly stays at the hollow site (97%) at the IS (see Table 1). This may be attributed to the fact that the hollow site adsorbed CO is less protruding outside the surface and thus interferes less with the existing H-bonding network in stabilizing OH.

The presence of O and OH species on the Pt surface will naturally lead to the system under the positive electrochemical potential conditions. For example, the CO + OH reaction in the

https://doi.org/10.1021/acscatal.2c01561
ACS Catal. 2022, 12, 6265−6275

aqueous solution is at 0.7 V from our DFT calculations by measuring the electrostatic potential of the system and referring to the absolute potential of the Pt electrode at 0 V (see Figure S2 for more details).[52−54] This allows us to compare the calculated reaction kinetics data with the relevant electrochemical experiments.

As for the free-energy profiles, the most striking finding is the high barrier of CO + OH in the aqueous surroundings, 0.76 eV at 300 K, compared to it under the solid−gas conditions, only 0.46 eV. This suggests that the reaction in the aqueous solution is 10^5 orders of magnitude slower than that in the gas phase. The presence of the water solution thus quenches the low-temperature CO oxidation. Nevertheless, this result explains the puzzling findings in experiments, where CO oxidation in the presence of a trace of H_2O occurs above ∼220 K under the solid−gas conditions, but CO is a poisoning species on Pt electrodes until the electrochemical potential is elevated to more than 0.4 V. Even in the presence of OH, the reaction rate of CO oxidation is not fast, that is, 0.57 s^{-1} in alkaline solution,[24] from the measured cyclic voltammogram curve, which agrees well with our calculated rate of 1.03 s^{-1} for the aqueous CO + OH at 300 K.

By using the free-energy barriers at different temperatures, we obtained the Arrhenius plots for the two aqueous reactions, as shown in Figure 3c,d. We found that compared to the solid−gas reactions, the reactions in the aqueous phase have the opposite trend of activity with respect to temperature: with the increase of temperature, the reaction has the lower free-energy barrier. For example, the free-energy barrier of CO + O in the aqueous phase is 0.91 eV at 300 K, close to that in the gas phase, but slightly decreases to 0.90 eV at 380 K. The trend is the same for CO + OH reaction, with the free-energy barrier decreasing from 0.76 eV at 300 K to 0.74 eV at 380 K. As a result, the pre-exponential factors for the reactions are generally larger than their counterparts in the gas phase, being 7.69 × 10^{13} s^{-1} and 2.97 × 10^{14} s^{-1} for the aqueous CO + O and CO + OH reactions, respectively. The activation entropy is derived to be 20.57 and 31.80 $J{\cdot}mol^{-1}{\cdot}K^{-1}$, both turning out to be positive, in contrast to those under the solid−gas conditions.

Despite the high barrier of CO + OH reaction in aqueous solution (0.76 eV) compared to the the solid−gas conditions, the reaction is still much faster than CO + O reaction in aqueous solution (a free-energy barrier of 0.91 eV, see Table 1): at 300 K, the rate differs by 373 times. We can thus conclude that the CO + OH reaction is always the dominant channel for CO oxidation in aqueous solution on Pt(111) terraces.

3.2.1. MD Trajectory Analysis. Our results reveal that the activation entropy of aqueous reactions is positive, just opposite to that under the solid−gas conditions. It is thus of interest to further analyze the MD trajectories for the aqueous CO + OH reaction by tracing the geometrical changes from IS to TS. Similar to that under the solid−gas conditions, we also computed the RDF, $g(r)$, for the C−Pt and O_a−Pt pairs, and the OH bond angle distribution and the results are shown in Figure 4d−f. Three major features for the aqueous reaction are thus revealed and they are elaborated in the following.

(i) The translation movement of CO at the IS is highly frustrated as reflected in the $g_{C-Pt}(r)$ plot, where the C−Pt first peak at the IS has no obvious tails, indicating that the hollow to bridge movement is largely blocked. Indeed, the population of CO at the bridge site is reduced to 3% from statistics, much lower than 34% under the solid−gas conditions. On the other hand, we note that the second peak (∼3−4 Å) is broader at the TS than at the IS, implying that CO at the TS, although at the top site, can have a large wagging displacement and thus interact dynamically with six nearby Pt atoms.

(ii) The OH is pinned well at the top site at both IS and TS since there is no splitting of the first peak for OH in the $g_{O-Pt}(r)$ plot. Similar to the finding for CO, the top OH can have a large wagging movement at the TS, leading to the broader successive peaks.

(iii) The rotation of the OH bond is no longer free even at the IS, which is limited by the H-bonding network to a small window centering at −120°, as shown in the probability distribution plot of the OH rotation angle. On the contrary, the rotation at the TS has one additional peak at +100°, suggesting that the OH bond has more degrees of freedom. Compared to the CO + OH reaction under the solid−gas conditions, the aqueous solution suppresses obviously the rotation of OH, particularly at the IS.

The above three findings all lead to the same conclusion that the configuration entropy of the aqueous reaction increases from IS to TS, and thus, the activation entropy is positive. The aqueous solution suppresses the translation/rotation degrees of freedom at the IS more than those at the TS. To understand the physical origin, we thus further analyzed the H-bonding network at the IS and the TS. Figure 5b shows the RDF for the O_a with its nearby H in water, $g_{O-H}(r)$ at the IS and the TS, which can reflect the change of the H-bondings around the O_a. A large, broad peak at 1.7 Å is present at the IS, indicating the presence of the H-bonding between O_a and neighboring water molecules, and this peak vanishes at the TS. This picture is consistent with the H-bonding snapshots (Figure 5a) taken at the IS and TS, focusing on the local environment of adsorbed OH. Obviously, the presence of H-bondings in the aqueous surroundings restricts strongly the translation of CO/OH and the rotation of OH at the IS, but the restriction is much released at the TS.

4. DISCUSSION

4.1. Free Energy of Surface Reactions. The free-energy barrier is the key kinetics quantity determining chemical reactivity. By using the G-NN potential-based US MD technique, we can now systematically evaluate the entropy contribution for CO oxidation reactions occurring with and without the aqueous surroundings, which can be of general significance for understanding catalytic reactions on surfaces *via* the Langmuir−Hinshelwood[15] mechanism. Two general lessons can be learned from our results.

First, the activation entropy of surface reactions is generally small even in the aqueous surroundings but can be critical to the reaction rate. The values for the four recombination reactions (CO + O(g), CO + OH(g), CO + O(aq), and CO + OH(aq)) are within ±35 $J{\cdot}mol^{-1}{\cdot}K^{-1}$, which is equivalent to ±0.1 eV at 300 K ($T\Delta S$). The neglection of the entropy term thus can lead to an error in rate by up to 48 times.

The configuration entropy contributes majorly to the activation entropy, while the vibrational entropy computed from harmonic approximation can be both wrong in the sign and smaller by 1 order of magnitude. Therefore, the common practice to estimate the reaction entropy *via* harmonic approximation appears to be a poor approximation for surface recombination reactions. On the other hand, we note that the free-energy computation *via* the US MD technique also has its

https://doi.org/10.1021/acscatal.2c01561
ACS Catal. 2022, 12, 6265−6275

own limitations, particularly to configure the reaction coordinate, which is still largely based on chemical intuition or trial-and-error approaches (*e.g.*, the C−O_a distance utilized in this work for CO oxidation). Without the correct reaction coordinate, the US MD can either fail to link the reaction pathway or produce the potential of mean force that is far off from the true free-energy profile.

Second, the major effect of the aqueous solution to surface reactions is still through the enthalpy term, where the presence of H-bonding near the surface can stabilize the reaction intermediates to different extents and thus alter the activity. The CO + OH reaction, as a good example, turns out to be much more difficult in the aqueous solution compared to the solid−gas conditions. Therefore, it is vital to identify the most stable configurations of reaction intermediates, both IS and TS, at the solid−liquid interface, based on which the reaction enthalpy can be computed accurately to predict the catalytic activity. In this sense, the long-time MD simulation and the constrained global optimization are important techniques to reveal these key thermodynamically favored structures in solution, which can now be significantly facilitated with the help of machine learning potentials.

4.2. Coverage Effect of CO Oxidation. Finally, we would like to discuss the coverage effect on CO oxidation. While this work, for better comparison, focuses on different CO oxidation reactions at the low coverage limit, one must bear in mind that the coverage of reactants is known to be critical to affect the kinetics. A striking evidence from experiments is the low-temperature CO oxidation on Pt(111) that occurs exclusively at the O island periphery after CO saturation coverage is reached.[11,13,55] The discrepancies in kinetics parameters measured from different experiments were also argued to be caused by the CO and O coverage and the domain size in the surface preparation procedure.[15,16,56]

To check the CO coverage effect, we have performed additional calculations by using the same theoretical approach. The main results are summarized below and the reaction snapshots for these high CO coverage reactions can be found in Figure S1.

(i) For the solid−gas CO + O reaction, when taking one CO molecule and one O coadsorbed in a $p(2 \times 2)$ unit cell (0.25 ML CO) as the IS, we obtained a free-energy barrier of 0.74 eV, which is 0.22 eV lower than that of the reaction occurring at 0.11 ML CO. This is apparently due to the initial CO adsorption site changing from hollow to top.

(ii) Further increasing CO coverage, when taking two CO and O coadsorbed in a $p(2 \times 2)$ unit cell (0.5 ML CO) as the IS, we obtained a free-energy barrier of 0.46 eV, being 0.28 eV lower than that of the reaction occurring at 0.25 ML CO.

(iii) Similarly, for the solid−liquid CO + OH reaction, when we increase the CO coverage to 0.25 ML (OH still at 0.06 ML), the free-energy barrier is also reduced to 0.65, 0.11 eV lower than that of the reaction with 0.06 ML CO coverage. This suggests that the reaction is much faster (~50 times) at the high coverage of CO. We found that at high CO coverages, the water layer is pushed away from the surface and both CO and OH can diffuse rapidly on the surface and thus the calculated barrier is close to the one (0.6 eV) under the solid−gas conditions of CO + OH reaction with a H_2O molecule nearby.[22]

The major reason for the change of free-energy barrier with coverage is the sensitivity of CO adsorption energy to the local CO and O coverage. Taking CO oxidation under the solid−gas reaction conditions as an example, from our DFT calculations, the CO adsorption energy drops from 1.68 eV at 0.25 ML coverage to 1.50 eV at 0.50 ML coverage (both at fcc hollow sites), indicating a repulsion interaction between adsorbed CO molecules. In the presence of the coadsorbed O atom (0.25 ML), we found that the CO adsorption energy drops more rapidly from 1.44 eV at 0.25 ML to 1.16 eV at 0.50 ML (the additional 0.25 ML CO occupies the hcp site). The large energy difference of 0.28 eV in the coadsorption case is consistent with the reduction in the barrier of CO oxidation from 0.74 at 0.25 ML to 0.46 eV at 0.5 ML.

From these results, we confirm that the CO coverage has strong influence on the CO oxidation kinetics no matter the presence of the aqueous surroundings. The effect (up to 0.5 eV from low coverage to the saturation coverage under the solid−gas conditions) can be much larger than the entropy contribution (~0.1 eV at 300 K). Considering that the kinetics data measured in experiments are the apparent value averages of all reaction situations with different CO and O/OH coverages, it is thus not surprising that the theoretical activation entropy of an elementary step at a well-defined coverage (condition) is generally far larger than the experimental values. We expect that the small pre-exponential factor in the experiment reflects the fact that the coverage of CO in the reaction is temperature-dependent and drops rapidly with the increase of temperature. More kinetics studies are needed to model CO oxidation at different coverages and at the domain boundaries.

5. CONCLUSIONS

To recap, this work reports the free-energy profiles for CO oxidation on Pt(111) *via* CO + O and CO + OH pathways under the solid−gas and solid−liquid reaction conditions. The first Pt−C−H−O G-NN is developed *via* self-learning of the SSW global optimization PES data. By combining the G-NN potential with US MD simulation, we determine the free-energy barriers of the reactions at different temperatures, based on which the activation entropies of reactions are derived from the Arrhenius plot. The physical origin of the activation entropy has been revealed by analyzing the MD trajectories to observe the configurational, translational, and rotational degrees of freedom. The key results are summarized as follows:

(i) The free-energy barriers are 0.96 for CO + O and 0.46 eV at 300 K for CO + OH reaction under the solid−gas conditions at the low coverage limit (0.11 ML CO and 0.11 ML O/OH). The activation entropies of the two reactions are negative, being −12.28 and −20.88 $J \cdot mol^{-1} \cdot K^{-1}$.

(ii) The free-energy barriers are 0.91 for CO + O and 0.76 eV at 300 K for CO + OH reaction in the aqueous solution at the low coverage limit (0.06 ML CO and 0.06 ML O/OH). The activation entropies of the two reactions are positive, being 20.57 and 31.80 $J \cdot mol^{-1} \cdot K^{-1}$. The aqueous solution introduces extra H-bondings to stabilize the adsorbed OH that significantly increases the barrier of CO + OH reaction compared to the solid−gas conditions. Despite this, the CO + OH reaction should still dominate CO oxidation on the Pt electrode under electrochemical conditions.

https://doi.org/10.1021/acscatal.2c01561
ACS Catal. 2022, 12, 6265−6275

(iii) The magnitudes of activation entropies (10−30 J·mol^{-1}·K^{-1}) are generally much larger than those of the vibrational entropies (0.4−2 J·mol^{-1}·K^{-1}) calculated from harmonic approximation, indicating that the configuration entropy dominates the activation entropy for the surface reactions.

(iv) CO oxidation activity is very sensitive to the CO coverage. For CO + O reaction under the solid−gas conditions, the free-energy barrier is reduced to 0.46 eV at 300 K with 0.5 ML CO and 0.25 ML O coverage. For CO + OH reaction in the aqueous solution, the free-energy barrier is reduced to 0.65 eV at 300 K with 0.25 ML CO and 0.06 ML OH coverage.

■ ASSOCIATED CONTENT

Supporting Information

The Supporting Information is available free of charge at https://pubs.acs.org/doi/10.1021/acscatal.2c01561.

G-NN potential architecture; SSW-NN method; calculation setups for DFT calculations; structural information of the most stable IS and TS from SSW-NN global optimization for all reactions investigated; more benchmark of G-NN against DFT calculations; reaction snapshots for reactions at high coverages; free-energy barriers from five US MD runs for different reactions; vibrational frequencies for all reactions at the IS and TS; electrochemical potential for CO + OH(aq) reaction on Pt(111); and *XYZ* coordinates for key reaction states (PDF)

■ AUTHOR INFORMATION

Corresponding Authors

Cheng Shang − *Collaborative Innovation Center of Chemistry for Energy Material, Shanghai Key Laboratory of Molecular Catalysis and Innovative Materials, Key Laboratory of Computational Physical Science, Department of Chemistry, Fudan University, Shanghai 200433, China; Shanghai Qi Zhi Institution, Shanghai 200030, China;* orcid.org/0000-0001-7486-1514; Email: cshang@fudan.edu.cn

Zhi-Pan Liu − *Collaborative Innovation Center of Chemistry for Energy Material, Shanghai Key Laboratory of Molecular Catalysis and Innovative Materials, Key Laboratory of Computational Physical Science, Department of Chemistry, Fudan University, Shanghai 200433, China; Shanghai Qi Zhi Institution, Shanghai 200030, China; Key Laboratory of Synthetic and Self-Assembly Chemistry for Organic Functional Molecules, Shanghai Institute of Organic Chemistry, Chinese Academy of Sciences, Shanghai 200032, China;* orcid.org/0000-0002-2906-5217; Email: zpliu@fudan.edu.cn

Authors

Ling-Heng Luo − *Collaborative Innovation Center of Chemistry for Energy Material, Shanghai Key Laboratory of Molecular Catalysis and Innovative Materials, Key Laboratory of Computational Physical Science, Department of Chemistry, Fudan University, Shanghai 200433, China*

Si-Da Huang − *Collaborative Innovation Center of Chemistry for Energy Material, Shanghai Key Laboratory of Molecular Catalysis and Innovative Materials, Key Laboratory of Computational Physical Science, Department of Chemistry, Fudan University, Shanghai 200433, China;* orcid.org/0000-0002-0055-1510

Complete contact information is available at: https://pubs.acs.org/10.1021/acscatal.2c01561

Notes

The authors declare no competing financial interest.

■ ACKNOWLEDGMENTS

This work was supported by the National Key Research and Development Program of China (2018YFA0208600), the National Science Foundation of China (12188101, 22033003, 91945301, 91745201, 92145302, 22122301, and 92061112), and the Tencent Foundation for XPLORER PRIZE.

■ REFERENCES

(1) Freund, H.-J.; Meijer, G.; Scheffler, M.; Schlögl, R.; Wolf, M. CO Oxidation as a Prototypical Reaction for Heterogeneous Processes. *Angew. Chem., Int. Ed.* **2011**, *50*, 10064−10094.

(2) Kummer, J. T. Use of noble metals in automobile exhaust catalysts. *J. Phys. Chem.* **1986**, *90*, 4747−4752.

(3) Bekyarova, E.; Fornasiero, P.; Kašpar, J.; Graziani, M. CO oxidation on Pd/CeO_2−ZrO_2 catalysts. *Catal. Today* **1998**, *45*, 179−183.

(4) Luo, M.-F.; Hou, Z.-Y.; Yuan, X.-X.; Zheng, X.-M. Characterization study of CeO_2 supported Pd catalyst for low-temperature carbon monoxide oxidation. *Catal. Lett.* **1998**, *50*, 205−209.

(5) Hopstaken, M. J. P.; Niemantsverdriet, J. W. Structure sensitivity in the CO oxidation on rhodium: Effect of adsorbate coverages on oxidation kinetics on Rh(100) and Rh(111). *J. Chem. Phys.* **2000**, *113*, 5457.

(6) Zheng, B.; Wu, S.; Yang, X.; Jia, M.; Zhang, W.; Liu, G. Room Temperature CO Oxidation over Pt/$MgFe_2O_4$: A Stable Inverse Spinel Oxide Support for Preparing Highly Efficient Pt Catalyst. *ACS Appl. Mater. Interfaces* **2016**, *8*, 26683−26689.

(7) Baschuk, J. J.; Li, X. Carbon monoxide poisoning of proton exchange membrane fuel cells. *Int. J. Energy Res.* **2001**, *25*, 695−713.

(8) Borup, R.; Meyers, J.; Pivovar, B.; Kim, Y. S.; Mukundan, R.; Garland, N.; Myers, D.; Wilson, M.; Garzon, F.; Wood, D.; Zelenay, P.; More, K.; Stroh, K.; Zawodzinski, T.; Boncella, J.; McGrath, J. E.; Inaba, M.; Miyatake, K.; Hori, M.; Ota, K.; Ogumi, Z.; Miyata, S.; Nishikata, A.; Siroma, Z.; Uchimoto, Y.; Yasuda, K.; Kimijima, K.-I.; Iwashita, N. Scientific Aspects of Polymer Electrolyte Fuel Cell Durability and Degradation. *Chem. Rev.* **2007**, *107*, 3904−3951.

(9) Bergeld, J.; Kasemo, B.; Chakarov, D. V. CO oxidation on Pt(111) promoted by coadsorbed H_2O. *Surf. Sci.* **2001**, *495*, L815−L820.

(10) Ratnasamy, C.; Wagner, J. P. Water Gas Shift Catalysis. *Catal. Rev.* **2009**, *51*, 325−440.

(11) Nakai, I.; Kondoh, H.; Amemiya, K.; Nagasaka, M.; Shimada, T.; Yokota, R.; Nambu, A.; Ohta, T. Mechanism of the CO oxidation reaction on O-precovered Pt(111) surfaces studied with near-edge x-ray absorption fine structure spectroscopy. *J. Chem. Phys.* **2005**, *122*, 134709.

(12) Kinne, M.; Fuhrmann, T.; Zhu, J. F.; Whelan, C. M.; Denecke, R.; Steinrück, H.-P. Kinetics of the CO oxidation reaction on Pt(111) studied by in situ high-resolution x-ray photoelectron spectroscopy. *J. Chem. Phys.* **2004**, *120*, 7113−7122.

(13) Wintterlin, J.; Völkening, S.; Janssens, T. V. W.; Zambelli, T.; Ertl, G. Atomic and Macroscopic Reaction Rates of a Surface-Catalyzed Reaction. *Science* **1997**, *278*, 1931−1934.

(14) Zaera, F.; Liu, J.; Xu, M. Isothermal study of the kinetics of carbon monoxide oxidation on Pt(111): Rate dependence on surface coverages. *J. Chem. Phys.* **1997**, *106*, 4204−4215.

(15) Campbell, C. T.; Ertl, G.; Kuipers, H.; Segner, J. A molecular beam study of the catalytic oxidation of CO on a Pt(111) surface. *J. Chem. Phys.* **1980**, *73*, 5862−5873.

(16) Gland, J. L.; Kollin, E. B. Carbon monoxide oxidation on the Pt(111) surface: Temperature programmed reaction of coadsorbed

atomic oxygen and carbon monoxide. *J. Chem. Phys.* **1983**, *78*, 963−974.
(17) Janthon, P.; Viñes, F.; Sirijaraensre, J.; Limtrakul, J.; Illas, F. Adding Pieces to the CO/Pt(111) Puzzle: The Role of Dispersion. *J. Phys. Chem. C* **2017**, *121*, 3970−3977.
(18) Alavi, A.; Hu, P.; Deutsch, T.; Silvestrelli, P. L.; Hutter, J. CO Oxidation on Pt(111): An Ab InitioDensity Functional Theory Study. *Phys. Rev. Lett.* **1998**, *80*, 3650−3653.
(19) Eichler, A. CO oxidation on transition metal surfaces: reaction rates from first principles. *Surf. Sci.* **2002**, *498*, 314−320.
(20) Grabow, L. C.; Gokhale, A. A.; Evans, S. T.; Dumesic, J. A.; Mavrikakis, M. Mechanism of the Water Gas Shift Reaction on Pt: First Principles, Experiments, and Microkinetic Modeling. *J. Phys. Chem. C* **2008**, *112*, 4608−4617.
(21) Gong, X.-Q.; Liu, Z.-P.; Raval, R.; Hu, P. A Systematic Study of CO Oxidation on Metals and Metal Oxides: Density Functional Theory Calculations. *J. Am. Chem. Soc.* **2004**, *126*, 8−9.
(22) Gong, X.-Q.; Hu, P.; Raval, R. The catalytic role of water in CO oxidation. *J. Chem. Phys.* **2003**, *119*, 6324−6334.
(23) Jørgensen, M.; Grönbeck, H. Adsorbate Entropies with Complete Potential Energy Sampling in Microkinetic Modeling. *J. Phys. Chem. C* **2017**, *121*, 7199−7207.
(24) Spendelow, J. S.; Goodpaster, J. D.; Kenis, P. J. A.; Wieckowski, A. Mechanism of CO Oxidation on Pt(111) in Alkaline Media. *J. Phys. Chem. B* **2006**, *110*, 9545−9555.
(25) Su, M.; Dong, J. C.; Le, J. B.; Zhao, Y.; Yang, W. M.; Yang, Z. L.; Attard, G.; Liu, G. K.; Cheng, J.; Wei, Y. M.; Tian, Z. Q.; Li, J. F. In Situ Raman Study of CO Electrooxidation on Pt(hkl) Single-Crystal Surfaces in Acidic Solution. *Angew. Chem., Int. Ed.* **2020**, *59*, 23554−23558.
(26) Kardash, D.; Huang, J.; Korzeniewski, C. Surface Electrochemistry of CO and Methanol at 25−75 °C Probed in Situ by Infrared Spectroscopy. *Langmuir* **2000**, *16*, 2019−2023.
(27) Fang, Y.-H.; Wei, G.-F.; Liu, Z.-P. Constant-Charge Reaction Theory for Potential-Dependent Reaction Kinetics at the Solid-Liquid Interface. *J. Phys. Chem. C* **2014**, *118*, 3629−3635.
(28) Huang, S.-D.; Shang, C.; Zhang, X.-J.; Liu, Z.-P. Material discovery by combining stochastic surface walking global optimization with a neural network. *Chem. Sci.* **2017**, *8*, 6327−6337.
(29) Huang, S.-D.; Shang, C.; Kang, P.-L.; Liu, Z.-P. Atomic structure of boron resolved using machine learning and global sampling. *Chem. Sci.* **2018**, *9*, 8644−8655.
(30) Torrie, G. M.; Valleau, J. P. Nonphysical sampling distributions in Monte Carlo free-energy estimation: Umbrella sampling. *J. Comput. Phys.* **1977**, *23*, 187−199.
(31) Behler, J. Representing potential energy surfaces by high-dimensional neural network potentials. *J. Phys.: Condens. Matter* **2014**, *26*, 183001.
(32) Shang, C.; Liu, Z.-P. Stochastic Surface Walking Method for Structure Prediction and Pathway Searching. *J. Chem. Theory Comput.* **2013**, *9*, 1838−1845.
(33) Shang, C.; Zhang, X.-J.; Liu, Z.-P. Stochastic surface walking method for crystal structure and phase transition pathway prediction. *Phys. Chem. Chem. Phys.* **2014**, *16*, 17845−17856.
(34) Shang, C.; Liu, Z.-P. LASP G-NN Potential. www.lasphub.com/supportings/PtCHO_pf_lhluo.pot (accessed April 04, 2022).
(35) Kästner, J.; Thiel, W. Bridging the gap between thermodynamic integration and umbrella sampling provides a novel analysis method: "Umbrella integration". *J. Chem. Phys.* **2005**, *123*, 144104.
(36) Rice, P. S.; Mao, Y.; Guo, C.; Hu, P. Interconversion of hydrated protons at the interface between liquid water and platinum. *Phys. Chem. Chem. Phys.* **2019**, *21*, 5932−5940.
(37) Bunting, R. J.; Rice, P. S.; Thompson, J.; Hu, P. Investigating the innate selectivity issues of methane to methanol: consideration of an aqueous environment. *Chem. Sci.* **2021**, *12*, 4443−4449.
(38) Kresse, G.; Furthmüller, J. Efficient iterative schemes for ab initio total-energy calculations using a plane-wave basis set. *Phys. Rev. B: Condens. Matter Mater. Phys.* **1996**, *54*, 11169−11186.
(39) Kresse, G.; Furthmüller, J. Efficiency of ab-initio total energy calculations for metals and semiconductors using a plane-wave basis set. *Comput. Mater. Sci.* **1996**, *6*, 15−50.
(40) Kresse, G.; Joubert, D. From ultrasoft pseudopotentials to the projector augmented-wave method. *Phys. Rev. B: Condens. Matter Mater. Phys.* **1999**, *59*, 1758−1775.
(41) Perdew, J. P.; Burke, K.; Ernzerhof, M. Generalized Gradient Approximation Made Simple. *Phys. Rev. Lett.* **1996**, *77*, 3865−3868.
(42) Vega, L.; Viñes, F. Generalized gradient approximation adjusted to transition metals properties: Key roles of exchange and local spin density. *J. Comput. Chem.* **2020**, *41*, 2598−2603.
(43) Grimme, S.; Antony, J.; Ehrlich, S.; Krieg, H. A consistent and accurate *ab initio* parametrization of density functional dispersion correction (DFT-D) for the 94 elements H-Pu. *J. Chem. Phys.* **2010**, *132*, 154104.
(44) Zhang, X.-J.; Shang, C.; Liu, Z.-P. Double-Ended Surface Walking Method for Pathway Building and Transition State Location of Complex Reactions. *J. Chem. Theory Comput.* **2013**, *9*, 5745−5753.
(45) Shang, C.; Liu, Z.-P. Constrained Broyden Dimer Method with Bias Potential for Exploring Potential Energy Surface of Multistep Reaction Process. *J. Chem. Theory Comput.* **2012**, *8*, 2215−2222.
(46) Bunluesin, T.; Gorte, R. J.; Graham, G. W. Studies of the water-gas-shift reaction on ceria-supported Pt, Pd, and Rh: Implications for oxygen-storage properties. *Appl. Catal., B* **1998**, *15*, 107−114.
(47) Roh, H.-S.; Jeong, D.-W.; Kim, K.-S.; Eum, I.-H.; Koo, K. Y.; Yoon, W. L. Single Stage Water-Gas Shift Reaction Over Supported Pt Catalysts. *Catal. Lett.* **2011**, *141*, 95−99.
(48) Sprowl, L. H.; Campbell, C. T.; Árnadóttir, L. Hindered Translator and Hindered Rotor Models for Adsorbates: Partition Functions and Entropies. *J. Phys. Chem. C* **2016**, *120*, 9719−9731.
(49) Liu, Z.-P.; Hu, P. General trends in the barriers of catalytic reactions on transition metal surfaces. *J. Chem. Phys.* **2001**, *115*, 4977−4980.
(50) Zhang, C. J.; Hu, P. Why Must Oxygen Atoms Be Activated from Hollow Sites to Bridge Sites in Catalytic CO Oxidation? *J. Am. Chem. Soc.* **2000**, *122*, 2134−2135.
(51) Wei, G.-F.; Liu, Z.-P. Optimum nanoparticles for electrocatalytic oxygen reduction: the size, shape and new design. *Phys. Chem. Chem. Phys.* **2013**, *15*, 18555.
(52) Fang, Y.-H.; Liu, Z.-P. Tafel Kinetics of Electrocatalytic Reactions: From Experiment to First-Principles. *ACS Catal.* **2014**, *4*, 4364−4376.
(53) Fang, Y.-H.; Liu, Z.-P. Mechanism and Tafel Lines of Electro-Oxidation of Water to Oxygen on RuO_2(110). *J. Am. Chem. Soc.* **2010**, *132*, 18214−18222.
(54) Filhol, J.-S.; Neurock, M. Elucidation of the Electrochemical Activation of Water over Pd by First Principles. *Angew. Chem., Int. Ed.* **2006**, *45*, 402−406.
(55) Nakai, I.; Kondoh, H.; Amemiya, K.; Nagasaka, M.; Nambu, A.; Shimada, T.; Ohta, T. Reaction-path switching induced by spatial-distribution change of reactants: CO oxidation on Pt(111). *J. Chem. Phys.* **2004**, *121*, 5035−5038.
(56) Xu, M.; Liu, J.; Zaera, F. Kinetic evidence for the dependence of surface reaction rates on the distribution of reactants on the surface. *J. Chem. Phys.* **1996**, *104*, 8825−8828.

https://doi.org/10.1021/acscatal.2c01561
ACS Catal. 2022, 12, 6265−6275